The minimum admissible detuning efficiency of MRI receive-only surface coils

Sina Marhabaie, Aimé Labbé, Bruno Quesson, Marie Poirier-Quinot

The Minimum Admissible Detuning Efficiency of MRI Receive-Only Surface Coils

Abstract

Background: The minimum admissible detuning efficiency of a receive coil is an essential parameter for coil designers. A receive coil with inefficient detuning leads to inhomogeneous B_1 during excitation. Previously proposed criteria for quantifying the detuning efficiency rely on indirect measurements and are difficult to implement.

Purpose: To present an alternative method to quantify the detuning efficiency of receive-only surface coils.

Study type: Theoretical study supported by simulations and phantom experiments.

Phantoms: Uniform spherical (100 mm diameter) and cylindrical (66 mm diameter) phantoms.

Field strength/sequence: Dual repetition time B_1 mapping sequence at 1.5 T, and Bloch-Siegert shift B_1 mapping sequence at 3.0 T.

Assessment: One non-planar (80 mm × 43 mm) and 2 planar (40 mm and 57 mm diameter) surface coils were built. Theoretical analysis was performed to determine the minimum detuning efficiency required to avoid B_1 distortions. Experimental B_1 maps were acquired for the non-planar and planar surface coils at both 1.5 T and 3.0 T and visually compared with simulated B_1 maps to assess the validity of the theoretical analysis.

Statistical tests: None.

Results: Based on the theoretical analysis, the proposed minimum admissible detuning efficiency, defined as DE_{thr} = 20 Log (Q) + 13 dB, depended only on the quality factor (Q) of the coil and was independent of coil area and field strength. Simulations and phantom experiments showed that when the detuning efficiency was higher than this minimum threshold level, the B_1 field generated by the transmission coil was not modified by the receive coil.

Data conclusion: The proposed criterion for assessing the detuning efficiency is simple to measure, and does not depend on the area of the coil or on the magnetic field strength, up to 3T. Experimental and simulated B_1 maps confirmed that detuning efficiencies above the theoretically derived minimal admissible detuning efficiency resulted in a non-distorted B_1 field.

Keywords:

B_1 distortion, B_1 inhomogeneity, Coil decoupling, Detuning, Detuning efficiency, Surface coil, Q factor, Quality factor

Introduction

Receive-only coils are essential components in state-of-the-art MRI scanners and provide higher signal-to-noise ratio (SNR) than volume coils (1), such as the body coil. Receive-only coils must be effectively detuned (or decoupled) during the transmission phase of an MR experiment or the current induced in the receive coil will produce an unwanted B_1 field (localized around the coil) that degrades the B_1 homogeneity and image quality (2). Furthermore, the induced current could significantly heat the coil and its surroundings, creating a potentially hazardous situation for the patients (3), particularly for intravascular coils.

Numerous methods have been proposed to detune a receive-only coil (Edelstein et al., 1986, Gruber et al., 2018, Mispelter et al., 2006), mainly using diodes (very often PIN diodes), an example of which is illustrated in Fig. 1(a). However, few studies have quantified the minimum admissible detuning efficiency in receive-only surface coils. Edelstein et al. (2) proposed that when the Q factor (quality factor) of the detuning circuit is much larger than the number of the capacitors used to resonate the surface coil, the coil is efficiently detuned. Kocharian et al. (6) defined a parameter called “artifact intensity” on MR images to assess decoupling efficiency and quantified it for surface coils of different sizes and blocking impedances. However, this approach is dependent on the area of the coil. Taracila et al. (7) quantified the B1 distortion of a typical surface coil considering the area of the coil and the blocking impedance and defined a threshold value for the impedance of the blocking circuit above which there were negligible B1 distortions. Larson (8) also studied the B1 distortions of phased array surface coils, exploring the effects of the impedance of the blocking network on the B1 distortion and deriving some design principles to minimize that B1 distortion.

All these approaches remain complex because they depend on many experimental factors such as the area of the coil (sometimes not well-defined for curved coils), the main magnetic field and the impedance of the blocking circuit that is measured indirectly. They also

require that the coil is built and tested in the MR environment, which is time consuming, expensive and impractical for coil designers.

Thus the aims of this study were first to develop a simple criterion that must be fulfilled in order to avoid B_1 distortion which depends only on an easily measurable quantity, the Q factor of the receive coil, and which takes into account the area of the surface coil, the impedance of the blocking circuit, and the Larmor frequency (B_0 field); and second to perform numerical simulations and phantom studies to test the criterion in a number of different coils at both 1.5 T and 3.0 T.

Theory

To interpret the detuning efficiency, the general properties of two coupled oscillators must be considered (9) . Once two circuits with close resonance frequencies f_0 are coupled together, they behave as a new system with two distinct resonance frequencies. If these two frequencies are far enough from the original resonance frequency (f_0) of the non-detuned coil, the coil will show a large impedance at f_0, and therefore, current circulation will be effectively prohibited during the transmission. To effectively detune a receive-only coil, this frequency shift must be maximized by carefully selecting the inductors and capacitors in the blocking circuit, as well as in the receive coil.

For an MRI coil, properties such as the resonance frequency, Q factor, and $B_1/\sqrt{power}$ can be easily measured in an RF bench test with a double-loop probe (10, 11) or equivalently with a single-loop probe (12). Often, the scattering parameter S_{12} (or differential S_{11} for a single-loop probe) is measured as a function of frequency. A typical S_{12} curve belonging to one of the surface coils studied here is shown in Fig. 1(b). The resonance frequency of the non-detuned coil, the two new resonance frequencies of the detuned coil, as well as the detuning efficiency of the coil are shown in Fig. 1(b). In this study, the detuning efficiency (*DE*, measured in dB

units) is defined as the difference between the S_{12} (or differential S_{11} for a single-loop probe) values of the non-detuned and the detuned coils at f_0.

In the following paragraphs, we derive a simplified expression for the minimum admissible detuning efficiency which could be applied to planar and non-planar surface coils with arbitrary shapes. In Supplemental data 1, as a supporting example, we consider the particular case of circular planar coils and by using a different approach we derive the same expression for the minimum admissible detuning efficiency.

The minimum admissible *DE*: general case of a surface coil with an arbitrary shape

Consider a surface coil positioned in the excitation field $\vec{B}_1^{p,+}$, expressed by Eq. 1, as shown in Fig. 2(a).

$$\vec{B}_1^{p,+}(t) = B_1(0)\, exp(j\omega_0 t) \tag{1}$$

where $B_1(0)$ is the amplitude, ω_0 is the Larmor angular frequency, $j^2 = -1$, and t is the time. In this article, we use complex representation of B_1 according to the convention mentioned in (Brown et al., 2014), that is the real part is the $\hat{x}$ component and the imaginary part is the $\hat{y}$ component. The field $\vec{B}_1^{p,+}(t)$ is the primary B_1 field generated by the transmit coil, which is assumed to be homogeneous in space and have a circular polarization (whenever it is needed in this article, we use the superscript + to emphasize that $\vec{B}_1^{p,+}$ is the positive circularly polarized term). During the transmission, the excitation field $\vec{B}_1^{p,+}$ induces a current in the receive coil, which generates a secondary field $\vec{B}_1^{s,+}$. The value of $\vec{B}_1^{s,+}$ depends on the exciting field $\vec{B}_1^{p,+}$, and the relative orientation between the receive coil and the transmit coil, and varies through the space. However, the ratio $\left|\vec{B}_1^{s,+}\right|/\left|\vec{B}_1^{p,+}\right|$—calculated at any given point—is independent of $\vec{B}_1^{p,+}$, and could be used to quantify relative B_1 distortions. For this, we define a parameter called *MD* (that stands for Maximal Distortion) that represents the maximum acceptable value for the quantity $\left|\vec{B}_1^{s,+}\right|/\left|\vec{B}_1^{p,+}\right|$ and whose value can be chosen by the coil designer depending on

the desired detuning performance. Therefore, our goal was to derive a criterion which would guarantee that $\left|\overline{\vec{B}_1^{s,+}}\right| / \left|\vec{B}_1^{p,+}\right| < MD$, where, $\left|\overline{\vec{B}_1^{s,+}}\right|$ is the averaged value of $\left|\vec{B}_1^{s,+}\right|$ over the region of interest. We start by calculating the flux $\varphi^{p,+}$ passing through the coil. According to Faraday's law of induction, the voltage $v(t)$ that is induced by the transmit coil into the receive coil positioned inside the exciting field $\vec{B}_1^{p,+}(t)$ can be calculated as:

$$v(t) = -\frac{d\varphi^{p,+}}{dt} = -\frac{d}{dt}\iint_{\substack{Entire \\ surface}} \vec{B}_1^{p,+}(t).d\vec{S} = -\iint_{\substack{Entire \\ surface}} \frac{d}{dt}\vec{B}_1^{p,+}(t).d\vec{S} \tag{2}$$

$$= -j\omega_0 \iint_{\substack{Entire \\ surface}} \vec{B}_1^{p,+}(t).d\vec{S} = -j\omega_0\varphi^{p,+}$$

The surface integration could be performed over any surface that encompasses the coil. In our notation the coefficient *j* indicates a 90-degree phase shift; e.g. in Eq. 2, the voltage $v(t)$ lags 90 degrees behind the flux $\varphi^{p,+}$. The secondary magnetic flux of a non-detuned coil, $\varphi^{s,+}$, generated by the induced current, is expressed as:

$$\varphi^{s,+} = \frac{1}{2}L\, i_{non-detuned} = \frac{1}{2}L\frac{v(t)}{r} = -L\frac{j\,\omega_0}{2r}\varphi^{p,+} = -j\frac{Q}{2}\varphi^{p,+} \tag{3}$$

Where $Q = L\,\omega_0/r$ is the quality factor, L is the inductance of the coil, r is the equivalent series resistance of the coil, and $i_{non\text{-}detuned}$ is the current circulating in the non-detuned coil. The additional factor $\frac{1}{2}$ accounts for the fact that the field generated by the coil is linearly polarized. The receive coil and its blocking circuit both resonate at ω_0, therefore, they represent a purely resistive impedance at ω_0. As a result, the current circulating in the non-detuned coil ($i_{non\text{-}detuned}$) and the current circulating in the detuned coil ($i_{detuned}$) are in phase. We can then compute the detuning efficiency (expressed in dB) as follows:

$$DE = -20\log\left(\frac{i_{detuned}}{i_{non-detuned}}\right) \tag{4}$$

Therefore, for a detuned coil we have:

$$\varphi^{s,+} = \frac{1}{2} L\, i_{detuned} = -j\frac{1}{2} 10^{-\frac{DE}{20}}\, Q\, \varphi^{p,+} \tag{5}$$

Which can be written as:

$$\iint_{\substack{Entire \\ surface}} \vec{B}_1^{s,+}(t).d\vec{S} = -\,j\frac{1}{2} 10^{-\frac{DE}{20}}\, Q \iint_{\substack{Entire \\ surface}} \vec{B}_1^{p,+}(t).d\vec{S} \tag{6}$$

The entire area of the surface coil is given by: $\iint_{\substack{Entire \\ surface}} \vec{n}.d\vec{S}$, where $\vec{n}$ is the normal vector. By dividing both sides of Eq. 6 by this total area, we have:

$$\frac{\iint_{\substack{Entire \\ surface}} \vec{B}_1^{s,+}(t).d\vec{S}}{\iint_{\substack{Entire \\ surface}} \vec{n}.d\vec{S}} = -j\frac{1}{2} 10^{-\frac{DE}{20}} Q\, \frac{\iint_{\substack{Entire \\ surface}} \vec{B}_1^{p,+}(t).d\vec{S}}{\iint_{\substack{Entire \\ surface}} \vec{n}.d\vec{S}} \tag{7}$$

For a function $f(t)$, the quantify $\frac{\int f(t)dt}{\int dt}$ represents the average value $\overline{f(t)}$. Therefore, Eq. 7 expresses the averaged value of $\left|\vec{B}_1^{s,+}\right|$ (over the entire surface that encompasses the receive-only coil) as a function of the average value of $\left|\vec{B}_1^{p,+}\right|$, which is assumed to be homogeneous over the entire region of interest ($\left|\overline{\vec{B}_1^{p,+}}\right| = \left|\vec{B}_1^{p,+}\right|$). Therefore, Eq. 7 simplifies as follows:

$$\left|\overline{\vec{B}_1^{s,+}}\right| = -j\frac{1}{2} 10^{-\frac{DE}{20}} Q\, \left|\vec{B}_1^{p,+}\right| \tag{8}$$

However, in MR experiments, for safety standards and also for practical reasons there is a minimum distance of approximately 1 cm between the tissue and the conductors of the coil (7). As a result, for almost all practical situations, the region of interest excludes the areas that are too close (less than 1 cm apart) to the coil conductors. Since the $\vec{B}_1^{s,+}$ field is larger in the areas close to the coil conductors than in the other areas, the $\left|\vec{B}_1^{s,+}\right|$ field averaged over such a region of interest ($\left|\overline{\vec{B}_{1,ROI}^{s,+}}\right|$) is smaller than the $\left|\vec{B}_1^{s,+}\right|$ field averaged over the entire surface of the coil ($\left|\overline{\vec{B}_1^{s,+}}\right|$). Therefore, we have:

$$\left|\overline{\vec{B}_{1,ROI}^{s,+}}\right| = \alpha \left|\overline{\vec{B}_1^{s,+}}\right| = -j\frac{\alpha}{2} 10^{-\frac{DE}{20}} Q\, \left|\vec{B}_1^{p,+}\right| \tag{9}$$

Where $\alpha = \frac{\left|\overline{\vec{B}_{1,ROI}^{s,+}}\right|}{\left|\overline{\vec{B}_1^{s,+}}\right|}$ is a factor between 0 and 1, and its exact value varies with the shape and dimensions of the coil. Following the arguments given in the Supplemental data 2, $\alpha \approx \frac{1}{2}$ is a suitable estimate for most practical cases occurring in MR imaging. Therefore, we have:

$$\frac{\left|\overline{\vec{B}_{1,ROI}^{s,+}}\right|}{\left|\vec{B}_1^{p,+}\right|} \approx \frac{1}{4}\, 10^{-\frac{DE}{20}}\, Q \tag{10}$$

By assuming that $\vec{B}_1^{s,+}$ varies smoothly and continuously over the region of interest, we can express:

$$\frac{\left|\overline{\vec{B}_{1,ROI}^{s,+}}\right|}{\left|\vec{B}_1^{p,+}\right|} \approx \frac{1}{4}\, 10^{-\frac{DE}{20}}\, Q \approx MD \Longrightarrow\ 10^{-\frac{DE}{20}}\, Q \approx 4\, MD \tag{11}$$

According to Eq. 11, for a given Q, there exists a theoretical threshold for detuning efficiency, called DE_{thr}, for which $\frac{\left|\overline{\vec{B}_{1,ROI}^{s,+}}\right|}{\left|\vec{B}_1^{p,+}\right|} \approx MD$. Taracila et al. (7) used a value of 5 % for *MD*. Based on our simulations and experimental results (see below), we chose a value of 8 % since detuning performances under this condition were considered to be sufficient in terms of image quality. Using this value and converting Eq. 11 into dB units leads to :

$$20\, log\left(\, 10^{-\frac{DE_{thr}}{20}}\, Q\right) = 20\, log(4\, MD) = 20\, log(0.32)$$

$$DE_{thr}(\text{dB}) \approx 20\, log(Q) + 10\ \text{dB} \tag{12}$$

Note that our calculations are based on the amplitude of $\vec{B}_1^{s,+}$. However, in MRI experiments, only the transverse components of $\vec{B}_1^{s,+}$ flips the magnetization. Thus, different scenarios may occur depending on the orientation of the imaging planes. For example, as one can see in Fig. 2(b), for the central axial slice, $\vec{B}_1^{s,+}$ has $\hat{x}$ and $\hat{y}$ components. This is not the case for coronal slices, in which there is always a $\hat{z}$ component. This, leads to more significant B_1 distortions for axial slices with respect to coronal slices having the same Q and DE.

Materials and Methods

Coil fabrication and MRI experiments

To validate our approach, which is independent from the magnetic field, and also the area and the shape of the coil, experiments were conducted at 1.5 T and 3.0 T (Larmor frequency of 63.9 MHz and 127.8 MHz, respectively), using surface coils with different shapes (circular planar or rectangular curved) and effective areas. The coil properties and brief experimental details are summarized in Table 1. The planar coil was taped directly on a spherical phantom consisting of a plastic sphere with an internal diameter of 100 mm and an external diameter of 116 mm. The rectangular curved coil was also directly taped on a cylindrical bottle with an outer diameter of 66 mm. Both phantoms were filled with a solution of Gadoteric Acid (Gd-DOTA, Dotarem, Guerbet, France) in deionized water with a concentration of 7.14×10^{-4} mol L^{-1}. A picture of the phantoms and coils is shown in Figs. 3(b)-(d).

TABLE 1

The shape of the coil	B_0 (T)	Dimensions (mm)	Effective area (cm^2)	Wire radius (mm)	The shape of the phantom	Imaging plane
circular planar	1.5	$\text{diameter} = 40$	12.6	1.25	spherical	coronal
circular planar	1.5	$\text{diameter} = 57$	25.0	1.25	spherical	coronal, axial
circular planar	3.0	$\text{diameter} = 57$	25.0	1.25	spherical	coronal, axial
rectangular curved	3.0	$80\ (length) \times 43\ (width)$	26.7	0.5	cylindrical bottle	coronal, axial

The experiments at 1.5 T were performed on a Philips—Best, the Netherlands—Achieva MRI scanner, and those at 3.0 T were conducted on a GE Healthcare Technologies Inc — Chicago, Illinois, USA—Signa PET/MRI scanner. Each receive coil was tuned at the Larmor frequency using appropriate ceramic capacitors (Exxelia—Pessac, France—CHB and SHB series, 500 Volts, non-magnetic). For this study, no preamplifier was integrated into the circuit

since we only needed a simple resonating coil without reception ability. In all experiments, the body coil was used as the transceiver coil. The equivalent circuit of a typical coil is depicted in Fig. 3(a). A dashed red rectangle surrounds the detuning circuit (the blocking circuit). Small soldering irons symbolize the contact points of the blocking circuit (A and B) in Fig. 3(a). To change the state of the coil between the non-detuned and detuned states, terminals A and B were either soldered or unsoldered. A non-magnetic adjustable resistance (detuning degradation resistance in Fig. 3(a), 0-500 Ohms, Vishay—Malvern, UAS—TSM4ZL501KR10) enabled different detuning efficiencies.

To change the *Q* factor of the receive coil, an energy-consuming component was added to the circuit which is represented by the *Q* degradation resistance in Fig. 3(a). In practice, for experiments of the rectangular curved coil *Q* degradation was achieved by adding some edible salts to the phantom fluid (solution conductivity of 10.86 $mS.cm^{-1}$), and for experiments of the circular planar coils it was achieved by utilizing a sub-circuit (detailed in the Supplemental data 3) that plays the role of the *Q* degradation resistance.

At both magnetic fields, multi-slice built-in gradient echo based sequences provided by the constructor were used to map the amplitude of the total B_1 field ($\vec{B}_1^{tot,+} = \vec{B}_1^{p,+} + \vec{B}_1^{s,+}$) in axial and coronal slices. For central slices, the imaging planes were located at the center of the coil, shown by dashed lines in Fig. 3 (b) and (d). In off-center slices, there was an offset of 12.5 mm (for circular planar coil) or 9.5 mm (for rectangular curved coil) between the imaging plane and the central slice. At 1.5 T, actual flip angle imaging (AFI (13), known as dual TR in Philips terminology) was used as the B_1 mapping sequence, and at 3.0 T, a Bloch-Siegert shift B_1 mapping sequence was utilized (14). The 1.5 T maps directly report the quantity $\left|\vec{B}_1^{tot,+}\right|/\left|\vec{B}_1^{p,+}\right|$ (in percentage) for each pixel. However, the 3.0 T maps report 10 × flip angle as the intensity of each pixel. For the 3.0 T maps, the quantity $\left|\vec{B}_1^{tot,+}\right|/\left|\vec{B}_1^{p,+}\right|$ was calculated (in percentage) using the free software ImageJ attention ref pas adaptée (magpylib). The mapping parameters

are summarized in Table 2.

TABLE 2

The shape of the coil	B_0 (T)	B_1 mapping sequence	Flip angle (degree)	Field of view (mm × mm)	Slice thickness (mm)	Matrix size	TE / TR (ms)	# of scans
circular planar	1.5	AFI	60	200 × 200	3.3	132 × 133	2.9 / 30.0*	2
circular planar	3.0	Bloch-Siegert shift	30	200 × 200	5.0	128 × 128	13.7 /23.0	16
rectangular curved	3.0	Bloch-Siegert shift	10	100 × 100	5.0	128 × 128	13.7/23.0	16

* In AFI, the parameter TR extension was 120.0 ms.

RF bench measurements

The resonance frequency, Q factor, and detuning efficiency of each surface coil were measured using standard methods (Darrasse and Kassab, 1993, 1993; Ginefri et al., 1999). For all measurements, the coil was taped on the phantom to take the loading effects of the phantom into account. The frequency response of each coil was recorded on a Rohde & Schwarz—Munich, Germany—ZNLE3 vector network analyzer (VNA) using homemade probes.

Simulations

For the circular planar coils, the inductance was calculated using the Pycoilib (15) package, and for the curved rectangular coil, the inductance was determined empirically by resonating the coil against a known capacitor. The coil currents were calculated using Eq. 15 (Supplemental data 1), and the coil magnetic fields were computed using Magpylib (16), a free Python library based on analytical (static) expressions. Simulations were implemented by assuming the same geometry (coil size, position, phantom size, etc.) as in the experiments. The Python code used

is provided in the supplementary materials accessible via the following link: https://zenodo.org/record/8388359.

Results

Fig. 4 shows the reference B_1 maps obtained using the mapping protocols detailed in Table 2 without any adjacent surface coil. Although the B_1 field of a body coil is supposed to be spatially homogeneous, small variations are observed. In all experimental maps, the measured B_1 at the center was slightly (up to 11%) larger than at the peripheries. For better visualization in Figs. 4-8 background noise (corresponding to the empty areas outside of the phantoms) has been masked (pale blue).

Fig. 5 shows simulated and experimental B_1 maps of the 57 mm circular planar coil, corresponding to coronal (central and off-center) and axial (central and off-center) slices mapped at 3.0 T. For each Q factor, the corresponding DE_{thr} was calculated using Eq. 12, and is written at the top each column of images. For the same detuning efficiency and Q factor, B_1 distortions in an axial slice were more severe than in a coronal slice. Note that, an accurate measurement of large detuning efficiencies (larger than 44 dB in our setup) is not possible if the Q factor of the coil is too low (lower than 54 in our setup) as for a coil with a small Q factor, the circulating current is smaller than the detection limit of our bench measurement setup. Therefore, for these coils (indicated by "Not Available" in Figs. 5, 6 and 8), only simulated B_1 maps are presented.

Fig. 6 shows the coronal experimental and simulated B_1 maps obtained at 1.5 T for 40 mm and 57 mm circular planar coils. For each Q factor, the corresponding DE_{thr} was calculated using Eq. 12. The results show similar features to those in the coronal slices in Fig. 5. For the reasons mentioned above, no experimental results could be presented for (Q = 35, DE = 51 dB) and (Q = 28, DE = 54 dB).

Fig. 7 shows the simulated and experimental B_1 maps of the 57 mm circular planar coil for axial slices mapped at 1.5 T. For each Q factor, the corresponding DE_{thr} was calculated using Eq. 12. As in Fig. 5, for the same detuning efficiency and Q factor, B_1 distortions in an axial slice were more severe than in a coronal slice. Note that the position of the coil in the maps shown in Fig. 7 is not necessarily the same in all maps (see figure caption).

Fig. 8 shows the simulated and experimental B_1 maps of the rectangular curved surface coil at 3.0 T. Two axial (central and off-center) slices and two coronal (central and off-center) slices are shown. Both experimental and simulated maps show similar behavior to the planar coils. For axial and coronal slices, the B_1 distortion patterns are different. In addition, for the same detuning efficiency and Q factor, B_1 distortions in the axial slices are more severe than in coronal slices.

Discussion

This study proposes a method for MRI coil designers to assess whether the receiver coil detuning is sufficient to avoid image degradation and potential hazardous situations for the patient, before practical implementation of the coil. Unlike previous approaches (2, 6–8), our method relies solely on the measurement of the coil Q factor and the desired MD (here set at 8%), and makes it applicable to different clinical field intensities, validated here up to 3.0T.

Three key assumptions were made to provide a practical criterion for DE_{th}: First, in absence of any receive coil, the B_1 field generated by the transmission coil is considered to be spatially homogeneous inside the phantom. At higher field strengths, such as 7.0 T, this assumption may not be valid any longer and require additional validation to account for dielectric effects (17). Second, in our simulations, we assumed an infinitely thin slice. Improvement of the simulations may incorporate more sophisticated modelling of the actual B_1 over the acquired slice (using provided mathematical description) to compare with experimental results from B_1 mapping

techniques. However, determination of DE_{thr} to ensure efficient coil detuning during transmission did not require such implementation. The third assumption relates to the thickness of the coil conductor relative to the coil size and a minimum distance between the coil and the phantom. While the former condition remains valid for the vast majority of receiver surface coils, the latter condition may not be satisfied in some particular configuration such as for endovascular coils (19, 20).

Taking into account these assumptions, the most stringent criterion to ensure efficient detuning is given by:

$$DE_{thr}(\text{dB}) \approx 20\,log(Q) + 13\ \text{dB} \qquad (13)$$

When using linearly polarized fields for excitation, 6dB must be added to the DE_{thr} values to account for the contribution of $\vec{B}_1^{p,-}$ component (that does not exists in circular polarization). Minor discrepancies between experiments and simulations were observed, attributed to field inhomogeneities and measurement precision limitations of the VNA.

Limitations

This study used an empirical MD threshold of 8%, but coil designers can opt for more stringent values, such as the 5% threshold proposed by Taracila et al. (7) . Based on our mathematical calculation, the value of DEthr increases by 4 dB compared to the one corresponding to a MD of 8%.

No quantitative comparison was performed between simulated and measured B_1 maps. Spatial integration of the B_1 field over the slice thickness and spatial distribution of the emitted B_1 within the sample may be included in simulations (18). However, this is expected to have minimal impact on DE_{thr} for typical surface coil dimensions and slice thickness involved in clinical MR-imaging.

Data provided in this study did not include in vivo experiments due to safety and ethical

considerations inherent to assessment of detuning efficiency for various coil configurations and field strengths. The good agreement between simulations and experimental results confirmed that the DE_{thr} computed from the Q factor of the coil is a relevant parameter to design receive surface coils that ensure good image quality and patient's safety.

Conclusion

In this study, a criterion to determine the minimum admissible detuning efficiency for receive-only surface coils with an arbitrary shape was proposed, which depended only on the Q factor of the receive coil.

Supplemental data 1: The particular case of circular planar surface coils

Now consider the particular case of a circular planar coil with an area $\vec{A} = A\hat{x}$, positioned in the B_1 field expressed by Eq. 1, as shown in Fig. 2(b). For this simple case, by direct calculation of the induced current, one can calculate the ratio $\left|\vec{B}_1^{s,+}\right|/\left|\vec{B}_1^{p,+}\right|$. According to Faraday's law of induction, for a non-detuned coil (of resistance r, inductance L, and quality factor Q) the induced current $i_{non\text{-}detuned}$, can be expressed as:

$$i_{non-detuned}\,(t) = \frac{v(t)}{r} = -\frac{1}{r}\frac{d\varphi}{dt} = -\frac{j\omega_0}{r}\,\vec{A}\cdot\vec{B}_1^{p,+}(t) = -\frac{jQ}{L}\vec{A}\cdot\vec{B}_1^{p,+}(t) \tag{14}$$

And for a detuned coil, following the same arguments used in Eq. 5, the induced current could be written as:

$$\left|i_{detuned}(t)\right| = \frac{10^{-\frac{DE}{20}}\,Q}{L}\left|\vec{A}\cdot\vec{B}_1^{p,+}(t)\right| \tag{15}$$

For a circular coil of internal radius a_0, the secondary field $\vec{B}_1^{s,+}(t)$ generated at the center of the coil is given by:

$$\left|\vec{B}_1^{s,+}(t)\right| = \frac{\mu_0}{2a_0}\frac{\left|i_{detuned}(t)\right|}{2} = \frac{\mu_0}{4\,a_0}\frac{10^{-\frac{DE}{20}}\,Q}{L}\left|\vec{A}\cdot\vec{B}_1^{p,+}(t)\right| \tag{16}$$

Where μ_0 is the magnetic permeability. Note that the additional factor $\frac{1}{2}\,(|i(t)|/2)$ accounts for the fact that only half of the field generated by the coil has a good polarization. For a typical surface coil that is made from a wire of radius a_{wire}, the inductance L is given by the following formula: (21)

$$L = \mu_0\,a_0\left\{\ln\left(\frac{8\,a_0}{a_{wire}}\right) - 2\right\} \tag{17}$$

Thus, for a circular coil the ratio $\left|\vec{B}_1^{s,+}\right|/\left|\vec{B}_1^{p,+}\right|$ can be expressed as:

$$\frac{\left|\vec{B}_1^{s,+}\right|}{\left|\vec{B}_1^{p,+}\right|} = \frac{\pi\,10^{-\frac{DE}{20}}\,Q}{4\,\left\{\ln\left(\frac{8\,a_0}{a_{wire}}\right) - 2\right\}} \tag{18}$$

In Eq. 18 the factor $\{\ln(8\,a_0/a_{wire}) - 2\}$ varies smoothly as a function of $\frac{a_0}{a_{wire}}$. For typical values of $a_0 \approx 28$ mm and $a_{wire} \approx 1.2$ mm, $\{\ln(8\,a_0/a_{wire}) - 2\} \approx \pi$. Therefore:

$$\frac{\left|\vec{B}_1^{s,+}\right|}{\left|\vec{B}_1^{p,+}\right|} \approx \frac{1}{4}\, 10^{-\frac{DE}{20}}\, Q \tag{19}$$

Eq. 19 was derived by assuming that $\frac{a_0}{a_{wire}} \approx 23$. To take the variations of $\frac{a_0}{a_{wire}}$ into account, we consider an uncertainty bound of $\pm$ 3 dB, that is $\frac{\left|\vec{B}_1^{s,+}\right|}{\left|\vec{B}_1^{p,+}\right|}$ is calculated using Eq. 19, and it will be readjusted (up to $\pm$ 3 dB) depending on $\frac{a_0}{a_{wire}}$. A simple calculation show that the interval $8 < \frac{a_0}{a_{wire}} < 80$ corresponds to an uncertainty bound of $\pm$ 3 dB. Such a large variation interval for $\frac{a_0}{a_{wire}}$ encompasses almost all practical configurations of the surface coils used in clinical MRI.

Equations 19 and 10 are similar, except that in Eq. 10, $\left|\overline{\vec{B}_{1,ROI}^{s,+}}\right|$ represents the $\left|\vec{B}_1^{s,+}\right|$ field averaged over the region of interest whereas in Eq.19, $\left|\vec{B}_1^{s,+}\right|$ represents the B_1 field at the center of the circular planar coil. Note that at far distances from the coil, the quantity $\left|\vec{B}_1^{s,+}\right|/\left|\vec{B}_1^{p,+}\right|$ is much smaller than in the center, and in the areas that are too close to the coil conductors, this quantity is much larger than in the center. However, we are not interested in these two areas because the coil is not sensitive at far distances, and for safety reasons, a minimum distance must always be kept between the living tissue and the coil conductors. Therefore, since $\vec{B}_1^{s,+}$ varies smoothly, we use the quantity $\left|\vec{B}_1^{s,+}\right|/\left|\vec{B}_1^{p,+}\right|$ calculated at the center, to derive the necessary criterion for having a negligible B_1 distortion for a typical circular planar coil. By rewriting Eq. 19 in dB units, the criterion $DE_{thr}(\text{dB}) \approx 20\,log(Q) + 10$ dB is obtained, which is the same as Eq. 12.

Supplemental data 2: Calculation of the factor α

In the Theory section, α was defined as $\frac{\left|\overline{\vec{B}_{1,ROI}^{s,+}}\right|}{\left|\overline{\vec{B}_{1}^{s,+}}\right|}$, and we assumed that $\alpha \approx \frac{1}{2}$, to be an appropriate approximation for this parameter. Note that according to Eq. 9, a $\pm$41% variation in α, (that corresponds to the interval $[\sqrt{2}\,\alpha\,, \frac{\alpha}{\sqrt{2}}]$), leads to an uncertainty bound of $\pm$3 dB for DE_{thr}. Since such a large variation encompasses almost all practical coil designs in clinical MRI, for our purpose, an estimation of α with an accuracy of $\pm$41% is considered to be sufficient. In order to estimate α, we considered a thin structure of an area that corresponded to the total area of our coil, and a thick structure of an area that corresponded to our region of interest. Since our region of interest excluded the areas that were less than approximately 1 cm from the coil conductors (as illustrated in Fig. 10), our thick structure had a diameter of approximately 2 cm. Such an approach allowed us to relate the parameter α to the inductance of these structures, which can be calculated more easily.

Figures 9(a) and 9(b) depict a thin and a thick circular coil respectively, with the same diameter, carrying the same current *i*. Both cross-hatched regions (representing the region in which the flux will be calculated) have almost the same area. One can directly calculate $\left|\overline{\vec{B}_{1}^{s,+}}\right|$ over the cross-hatched regions. Note that, the integral $\iint_{\substack{Cross-hatched \\ in\ Fig.\ 9(a)}} \vec{B}_{1}^{s,+}.d\vec{S}$ is the total flux passing through the coil. Therefore we have:

$$\frac{\left|\overline{\vec{B}_{1,THICK\ CIRCLE}^{s,+}}\right|}{\left|\overline{\vec{B}_{1,THIN\ CIRCLE}^{s,+}}\right|} = \frac{\dfrac{\iint_{\substack{Cross-hatched \\ in\ Fig.\ 9(b)}} \vec{B}_{1}^{s,+}.d\vec{S}}{\iint_{\substack{Cross-hatched \\ in\ Fig.\ 9(b)}} \vec{n}.d\vec{S}}}{\dfrac{\iint_{\substack{Cross-hatched \\ in\ Fig.\ 9(a)}} \vec{B}_{1}^{s,+}.d\vec{S}}{\iint_{\substack{Cross-hatched \\ in\ Fig.\ 9(a)}} \vec{n}.d\vec{S}}} \approx \frac{\iint_{\substack{Cross-hatched \\ in\ Fig.\ 9(b)}} \vec{B}_{1}^{s,+}.d\vec{S}}{\iint_{\substack{Cross-hatched \\ in\ Fig.\ 9(a)}} \vec{B}_{1}^{s,+}.d\vec{S}} \tag{20}$$

$$\approx \frac{\varphi_{THICK\ CIRCLE}}{\varphi_{THIN\ CIRCLE}} \approx \frac{i\,L_{THICK\ CIRCLE}}{i\,L_{THIN\ CIRCLE}} \approx \frac{L_{THICK\ CIRCLE}}{L_{THIN\ CIRCLE}}$$

Equation 20 represents a simple relation to estimate α for a circular coil. By analogy, we can deduce that for a given coil with an arbitrary shape, α is the ratio of the inductance of the corresponding thick and thin structures, that is $\alpha \approx \frac{L_{THICK\ STRUCTURE}}{L_{THIN\ STRUCTURE}}$. For some regular shapes these inductances can be calculated using analytical formulas. For example, as illustrated in Figs. 9(a) and 9(b), for a circular coil $\alpha \approx \frac{L_{THICK\ CIRCLE}}{L_{THIN\ CIRCLE}} = \frac{106}{237} = 0.45$, and as illustrated in Figs. 9(c) and 9(d), for a rectangular coil $\alpha \approx \frac{L_{THICK\ RECTANGLE}}{L_{THIN\ RECTANGLE}} = \frac{81.2}{223} = 0.36$. Note that a given surface coil with an arbitrary shape can be considered as a series combination of several small pieces of straight wires. Therefore, by dividing an arbitrary coil into *N* small pieces of straight wires with identical lengths, and by neglecting any mutual effects between the small wires (since we do not seek a precise calculation):

$$\alpha = \frac{\left|\overline{\vec{B}^{s,+}_{1,THICK\ STRUCTURE}}\right|}{\left|\overline{\vec{B}^{s,+}_{1,THIN\ STRUCTURE}}\right|} \approx \frac{L_{THICK\ STRUCTURE}}{L_{THIN\ STRUCTURE}} \approx \frac{\sum L_{THICK\ WIREs}}{\sum L_{THIN\ WIREs}} \approx \frac{N}{N}\frac{L_{THICK\ WIRE}}{L_{THIN\ WIRE}} \approx \frac{L_{THICK\ WIRE}}{L_{THIN\ WIRE}} \tag{21}$$

Therefore, from the situation illustrated in Figs. 9(e) and 9(f), it can be deduced that for a coil with an arbitrary shape, $\alpha \approx \frac{1}{2}$. Note that many different approximations have been used thus far, and a lot of other factors have been neglected to derive Eq. 21. These approximations are valid except for a structure where the conductor is so thick that the effective areas of the thin and thick structures are substantially different. This is not the case for practical situations encountered in MRI. In Fig. 9, the calculated α values lie between 0.36 and 0.51, which are indeed inside the authorized interval of $[\frac{1}{2} \times \frac{1}{\sqrt{2}} = 0.35$ and $\frac{1}{2} \times \sqrt{2} = 0.70]$, corresponding to an uncertainty bound of ± 3 dB.

Supplemental data 3: The *Q* degradation sub-circuit

In some experiments, a sub-circuit that plays the role of the *Q* degradation resistance in Fig. 3(a) was used to reduce the *Q* factor of the receive coil. The *Q* degradation sub-circuit was a piece of a coaxial cable terminated with a parallel combination of capacitors, inductors and resistances. The length of the coaxial cable, the terminating resistance, inductor and capacitor were chosen so that the cable represented a purely resistive impedance at the Larmor frequency. It neither resonated nor appreciably coupled to the coil, and its sole effect was the reduction of the *Q* factor of the receive coil. To achieve different *Q* factors, the terminating capacitor or resistance could be changed, or another cable with a different thickness or length chosen. As an example, the components used in the *Q* degradation sub-circuit for experiment performed at 1.5 T are shown in Table 3. Note that this method was designed to avoid changing the phantom fluid (with different salt concentrations) for each experiment. However, since it is quite complicated, adding some edible salts to the phantom fluid (and changing the fluid for each experiment) may be preferred for degrading the *Q* factor of a receive coil.

TABLE 3

Coil diameter	***Q* factor**	***Capacitance value***	***Inductance value***	**Resistance value**	***Cable type and length***
40 mm	35	no capacitance	133 nH	560 Ω	RG316/32 cm
40 mm	110	1 nF	no inductance	25 Ω	RG316/32 cm + RG58/41 cm
57 mm	28	no capacitance	133 nH	620 Ω	RG316/32 cm
57 mm	94	1 nF	no inductance	25 Ω	RG316/32 cm + RG58/41 cm

References

1. Brown RW, Cheng Y-CN, Haacke EM, Thompson MR, Venkatesan R (Eds): *Magnetic Resonance Imaging: Physical Principles and Sequence Design*. Chichester, UK: John Wiley & Sons Ltd; 2014.

2. Edelstein WA, Hardy CJ, Mueller OM: Electronic Decoupling of Surface-Coil Receivers for NMR Imaging and Spectroscopy. *J Magn Reson* 1986; 67:156–161.

3. Dempsey MF, Condon B, Hadley DM: Investigation of the factors responsible for burns during MRI. *J Magn Reson Imaging* 2001; 13:627–631.

4. Gruber B, Froeling M, Leiner T, Klomp DWJ: RF coils: A practical guide for nonphysicists: RF Coils. *J Magn Reson Imaging* 2018; 48:590–604.

5. Mispelter J, Lupu M, Briguet A: *NMR Probeheads for Biophysical and Biomedical Experiments: Theoretical Principles & Practical Guidelines*. London : Hackensack, NJ: Imperial College Press ; Distributed by World Scientific; 2006.

6. Kocharian A, Rossman PJ, Hulshizer TC, Felmlee JP, Riederer SJ: Determination of appropriate RF blocking impedance for MRI surface coils and arrays. *Magn Reson Mater Phys Biol Med* 2000; 10:80–83.

7. Taracila V, Chan P, Robb F: Minimal Acceptable Blocking Impedance for RF receive coils. *Proc ISMRM P 3928* 2010.

8. Larson CK: Improving MRI Surface Coil Decoupling to Reduce B1 Distortion. University of Wisconsin Milwaukee; 2014.

9. Fletcher NH, Rossing TD: *The Physics of Musical Instruments*. New York, NY: Springer New York; 1998.

10. Darrasse L, Kassab G: Quick measurement of NMR-coil sensitivity with a dual-loop probe. *Rev Sci Instrum* 1993; 64:1841–1844.

11. Haase J, Curro NJ, Slichter CP: Double Resonance Probes for Close Frequencies. *J Magn Reson* 1998; 135:273–279.

12. Ginefri JC, Durand E, Darrasse L: Quick measurement of nuclear magnetic resonance coil sensitivity with a single-loop probe. *Rev Sci Instrum* 1999; 70:4730–4731.

13. Yarnykh VL: Actual flip-angle imaging in the pulsed steady state: A method for rapid three-dimensional mapping of the transmitted radiofrequency field. *Magn Reson Med* 2007; 57:192–200.

14. Sacolick LI, Wiesinger F, Hancu I, Vogel MW: B1 mapping by Bloch-Siegert shift. *Magn Reson Med* 2010; 63:1315–1322.

15. Labbé A, Poirier-Quinot M: Pycoilib: a free and pedagogical tool for the calculiaton of self/mutual inductance of coils of arbitrary geometry in python. London; 2022.

16. Ortner, M., Bandeira, L.G.C: Magpylib: A free Python package for magnetic field

computation. 2020.

17. Cloos MA, Knoll F, Zhao T, et al.: Multiparametric imaging with heterogeneous radiofrequency fields. *Nat Commun* 2016; 7:12445.

18. Frass-Kriegl R, Hosseinnezhadian S, Poirier-Quinot M, Laistler E, Ginefri J-C: Multi-Loop Radio Frequency Coil Elements for Magnetic Resonance Imaging: Theory, Simulation, and Experimental Investigation. *Front Phys* 2020; 7:237.

19. Kardoulaki EM, Syms RRA, Young IR, Rea M, Gedroyc WMW: Thin-film micro-coil detectors: Application in MR-thermometry. *Sens Actuators Phys* 2015; 226:48–58.

20. Homagk A-K, Umathum R, Korn M, et al.: An expandable catheter loop coil for intravascular MRI in larger blood vessels. *Magn Reson Med* 2010; 63:517–523.

21. Walter G: Theoretische Physik. *Harri Dtsch* 1991.

Figure Legends

Figure 1: (a) A typical design for classic detuning of a receive-only coil. The TR switch (usually a PIN diode) is closed during the transmission. Therefore, the auxiliary capacitor (C_{aux}) and the detuning inductor (L_{detune}) form a parallel resonant circuit, which resonates at ω_0, and thus has a huge impedance at ω_0. In this situation, the current that can circulate in the receive coil (shown as a small brown arrow), is much less than the current that otherwise circulates if the coil is not detuned (shown as a large green arrow). During the reception phase, the TR switch is open, and the coil remains tuned. (b) The frequency response of a typical surface receive coil. The green curve: S_{12} curve obtained by a double-loop probe when the coil is not detuned. Note that there is only one resonance around 64 MHz. The brown curve: the S_{12} curve obtained by the same double-loop probe at the same relative position with respect to the coil when the coil is detuned. Note that there are two resonances at around 22 and 78 MHz. The detuning efficiency (depicted as a red double-headed arrow) is the difference between the green and the brown curves at the

frequency of interest, here 64 MHz. Similar curves of differential S_{11} could be obtained using a single-loop probe.

Figure 2: Three-dimensional illustration of the relative position of a surface coil with an arbitrary shape (a), and a circular planar surface coil (b). The coils are located inside the transmit (body) coil, and the alternating magnetic field B_1 components are shown. The dashed black line represents the interface between the axial (*xy*) and coronal (*xz*) planes. The primary $\vec{B}_1^{p,+}$ field generated by the body coil is shown in blue and lies inside the axial plane. Both of its components can flip the magnetization. The secondary B_1 field generated by the surface coil, $\vec{B}_1^{s}$, is shown by two dashed arrows in blue for an axial slice located at the center of the surface coil, and in gray for a coronal slice located at the center of the surface coil. For an axial slice, both components of $\vec{B}_1^{s}$ can flip the magnetization. However, only the $\hat{x}$ component can flip the magnetization for the central coronal slice.

Figure 3: The equivalent circuit of a typical coil used in our experiments (a). The spherical phantom used in this study (b), and its position inside the MRI scanner (c). The rectangular curved coil on a bottle with an outer diameter of approximately 66 mm (d). The coil shown in (a) comprises a loop made from copper wire and two ceramic capacitors. The capacitors C_{tune} and C_{aux}, as well as the inductor L_{detune} are chosen so that both the receive coil and the detuning circuit (shown in the dashed red rectangle) resonate at the Larmor frequency. A variable resistance in series with L_{detune} is used to degrade the detuning efficiency, the larger this resistance, the smaller the detuning efficiency. To decrease the *Q* factor of the coil, either some edible salts were added to the phantom fluid, or a sub-circuit (explained in the Supplemental data 3) that plays the role of the *Q* degradation resistance was utilized. Small soldering irons

symbolize the contact points of the blocking circuit (A and B). To change the status of the coil between the non-detuned and detuned states, terminals A and B were either soldered or unsoldered. In (b) and (d) the vertical dashed lines represent the position of the central axial slices, and the horizontal dashed lines represent the position of the central coronal slices in our experiments. Electronic components in (a) are also shown in (b) using the same colors. The direction of the B_0 field is shown to illustrate the relative orientation of the phantom inside the scanner.

Figure 4: Reference B_1 maps of the phantom alone without any adjacent surface coils. These color maps indicate the quantity $B_1^{measured}/B_1^{nominal}$ in percentage terms. A coronal slice obtained at 1.5 T (a), a coronal slice obtained at 3.0 T (b), and an axial slice obtained at 3.0 T (c). Note that only the region of interest is shown, and background noise has been masked (pale blue).

Figure 5: Experimental and simulated B_1 maps for the 57 mm planar coil at 3.0 T. These color maps indicate the quantity $B_1^{measured}/B_1^{nominal}$ in percentage terms. The maps in each column correspond to the same Q factor which is indicated at the top of each column. The maps in each row correspond to the same detuning efficiency which is written on the left side of each row. The simulated map below each experimental map corresponds to the same Q factor and detuning efficiency as the experimental map. For central slices, the imaging planes were located at the center of the circular-planar coil (symmetry plane of the coil, shown by dashed lines in Fig. 3(b)). In off-center slices, there was an offset of 12.5 mm between the imaging plane and the center of the coil. For both axial and coronal slices, the DE_{thr} of each coil is calculated using Eq. 12, and is written on the top of the corresponding column. Note that an accurate

measurement of large detuning efficiencies is not possible if the Q factor is too low. Therefore in these cases the experimental maps are not available (see the results section for more explanation). Background noise in all experimental maps has been masked (pale blue).

Figure 6: Experimental and simulated coronal B_1 maps for the 40 mm (left) and 57 mm (right) circular planar coils at 1.5 T. These color maps indicate the quantity $B_1^{measured}/B_1^{nominal}$ in percentage terms. The maps in each column correspond to the same Q factor which is indicated at the top of each column. The maps in each row correspond to the same detuning efficiency which is written on the left side of each row. The simulated map below each experimental map corresponds to the same Q factor and detuning efficiency as the experimental map. The corresponding DE_{thr} of each coil is calculated using Eq. 12, and is written on the top of the corresponding column. Note that an accurate measurement of large detuning efficiencies is not possible if the Q factor is too low. Therefore in these cases the experimental maps are not available (see the results section for more explanation). Background noise in all experimental maps has been masked (pale blue).

Figure 7: Experimental and simulated axial B_1 maps of the 57 mm circular planar coil at 1.5 T. These color maps indicate the quantity $B_1^{measured}/B_1^{nominal}$ in percentage terms. The Q factor, and detuning efficiency of each coil are indicated at the top of each column. The corresponding DE_{thr} of each coil is calculated using Eq. 12, and is written between the simulated and experimental maps. The simulated map below each experimental map corresponds to the same Q factor and detuning efficiency as the experimental map. Note that in the left column, the coil was at the left side of the phantom (and also the left side of the image), but in the middle and

the right columns it was at the bottom of the phantom (and also the bottom of the image). Background noise in the experimental maps has been masked (pale blue).

Figure 8: Experimental and simulated B_1 maps of the rectangular curved (non-planar) surface coil shown in Fig. 3(d) at 3.0 T. These color maps indicate the quantity $B_1^{measured}/B_1^{nominal}$ in percentage terms. The maps in each column correspond to the same Q factor which is indicated at the top of each column. The maps in each row correspond to the same detuning efficiency which is written on the left side of each row. The simulated map below each experimental map corresponds to the same Q factor and detuning efficiency as the experimental map. For central slices, the imaging plane was located at the center of the circular-planar coil (symmetry plane of the coil, shown by dashed lines in Fig. 3(d)). In off-center slices, there was an offset of 9.5 mm between the imaging plane and the center of the coil. For both axial and coronal slices, the DE_{thr} of each coil is calculated using Eq. 12, and is written on the top of the corresponding column. Note that an accurate measurement of large detuning efficiencies is not possible if the Q factor is too low. Therefore in these cases the experimental maps are not available (see the results section for more explanation). Background noise in the experimental maps has been masked (pale blue).

Figure 9: The illustration of three thin and thick structures used to estimate the parameter α. The conductor has a circular cross-section of 2.5 mm diameter (top) or 20 mm (bottom) in all

structures. The inductance of each structure has been calculated using the inductance calculator freely provided by: https://www.eeweb.com.

Figure 10: A surface coil with an arbitrary shape. The coil is positioned inside a volume transmit coil such that the primary $\vec{B}_1^{p,+}$ field of the transmit coil can induce a current. This induced current generates a secondary $\vec{B}_1^{s,+}$ field much larger in the areas close to the coil conductors. Note the large and small arrows indicating different amplitude and direction of $\vec{B}_1^{s}$ at different areas. Note that the *yz* view of the coil is shown for better illustration, which is different to that shown in Fig. 2(a).

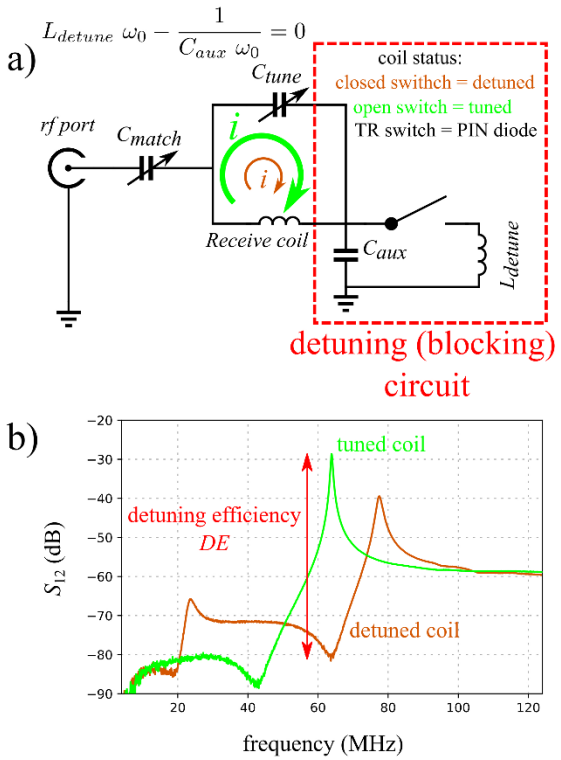

Figure 1: (a) A typical design for classic detuning of a receive-only coil. The TR switch (usually a PIN diode) is closed during the transmission. Therefore, the auxiliary capacitor (C_{aux}) and the detuning inductor (L_{detune}) form a parallel resonant circuit, which resonates at ω_0, and thus has a huge impedance at ω_0. In this situation, the current that can circulate in the receive coil (shown as a small brown arrow), is much less than the current that otherwise circulates if the coil is not detuned (shown as a large green arrow). During the reception phase, the TR switch is open, and the coil remains tuned. (b) The frequency response of a typical surface receive coil. The green curve: S_{12} curve obtained by a double-loop probe when the coil is not detuned. Note that there is only one resonance around 64 MHz. The brown curve: the S_{12} curve obtained by the same double-loop probe at the same relative position with respect to the coil when the coil is detuned. Note that there are two resonances at around 22 and 78 MHz. The detuning efficiency (depicted as a red double-headed arrow) is the difference between the green and the brown curves at the frequency of interest, here 64 MHz. Similar curves of differential S_{11} could be obtained using a single-loop probe.

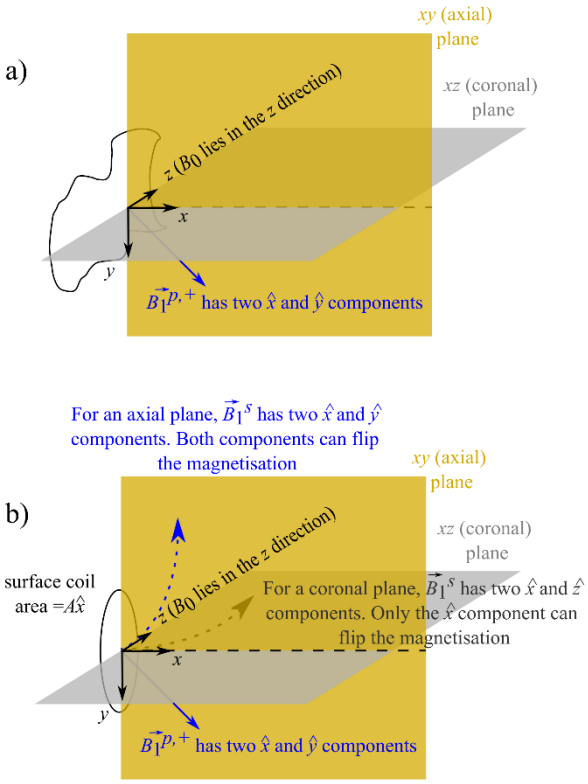

Figure 2: Three-dimensional illustration of the relative position of a surface coil with an arbitrary shape (a), and a circular planar surface coil (b). The coils are located inside the transmit (body) coil, and the alternating magnetic field B_1 components are shown. The dashed black line represents the interface between the axial (xy) and coronal (xz) planes. The primary $\vec{B}_1^{p,+}$ field generated by the body coil is shown in blue and lies inside the axial plane. Both of its components can flip the magnetization. The secondary B_1 field generated by the surface coil, $\vec{B}_1^{s}$, is shown by two dashed arrows in blue for an axial slice located at the center of the surface coil, and in gray for a coronal slice located at the center of the surface coil. For an axial slice, both components of $\vec{B}_1^{s}$ can flip the magnetization. However, only the $\hat{x}$ component can flip the magnetization for the central coronal slice.

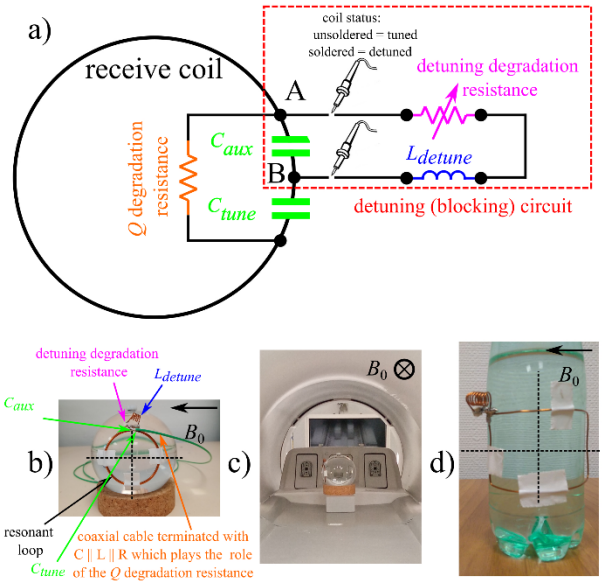

Figure 3: The equivalent circuit of a typical coil used in our experiments (a). The spherical phantom used in this study (b), and its position inside the MRI scanner (c). The rectangular curved coil on a bottle with an outer diameter of approximately 66 mm (d). The coil shown in (a) comprises a loop made from copper wire and two ceramic capacitors. The capacitors C_{tune} and C_{aux}, as well as the inductor L_{detune} are chosen so that both the receive coil and the detuning circuit (shown in the dashed red rectangle) resonate at the Larmor frequency. A variable resistance in series with L_{detune} is used to degrade the detuning efficiency, the larger this resistance, the smaller the detuning efficiency. To decrease the Q factor of the coil, either some edible salts were added to the phantom fluid, or a sub-circuit (explained in the Supplemental data 3) that plays the role of the Q degradation resistance was utilized. Small soldering irons symbolize the contact points of the blocking circuit (A and B). To change the status of the coil between the non-detuned and detuned states, terminals A and B were either soldered or unsoldered. In (b) and (d) the vertical dashed lines represent the position of the central axial slices, and the horizontal dashed lines represent the position of the central coronal slices in our experiments. Electronic components in (a) are also shown in (b) using the same colors. The direction of the B_0 field is shown to illustrate the relative orientation of the phantom inside the scanner.

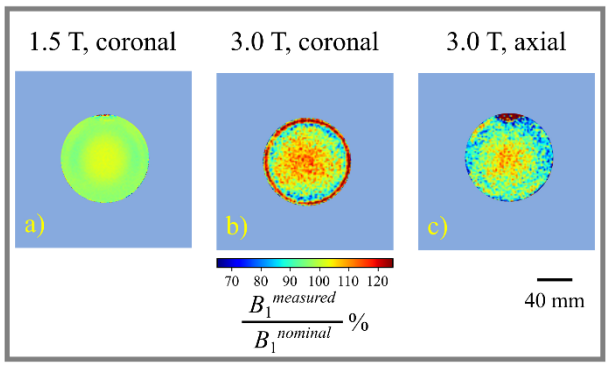

Figure 4: Reference B_1 maps of the phantom alone without any adjacent surface coils. These color maps indicate the quantity $B_1^{measured}/B_1^{nominal}$ in percentage terms. A coronal slice obtained at 1.5 T (a), a coronal slice obtained at 3.0 T (b), and an axial slice obtained at 3.0 T (c). Note that only the region of interest is shown, and background noise has been masked (pale blue).

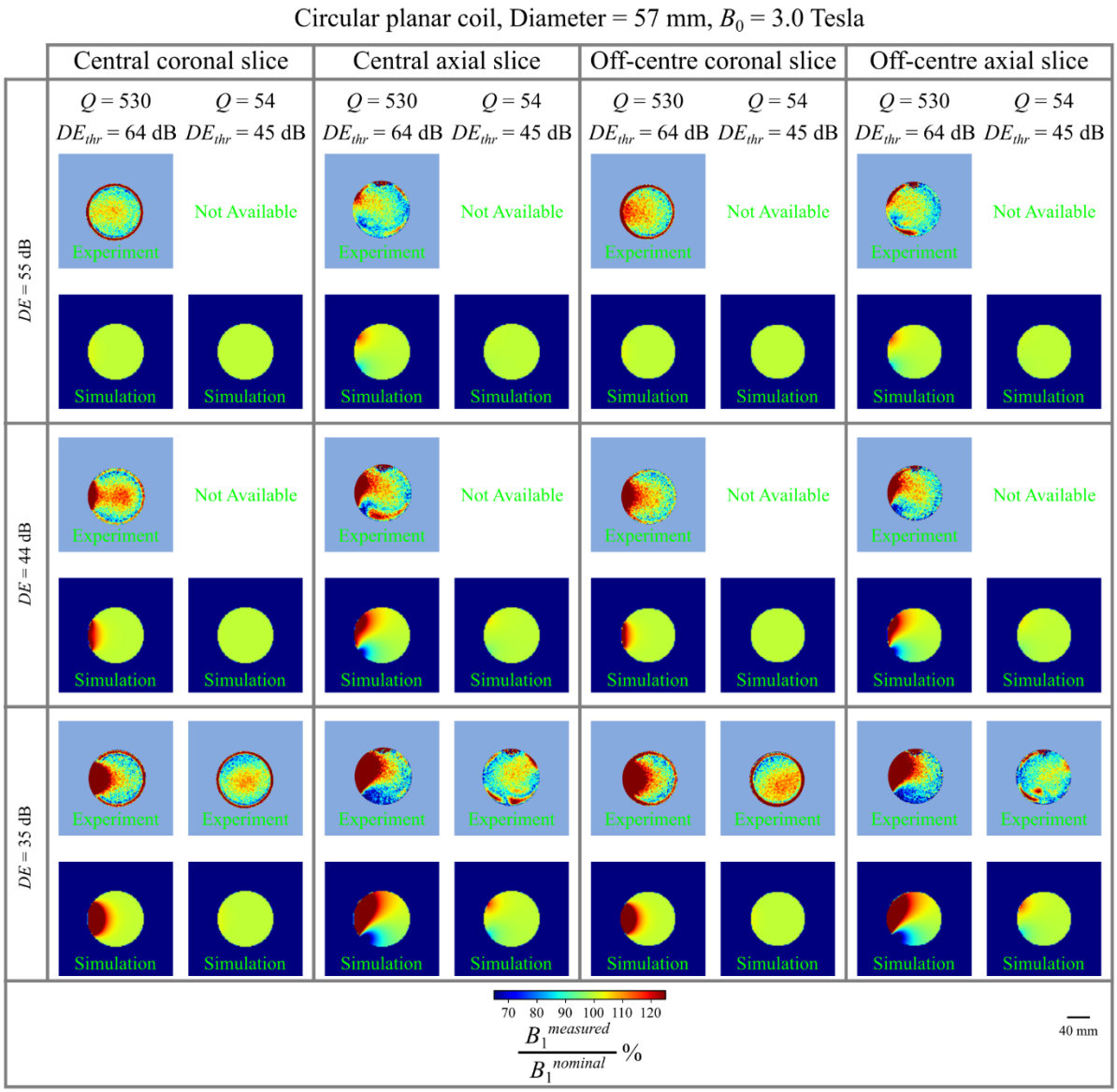

Figure 5: Experimental and simulated B_1 maps for the 57 mm planar coil at 3.0 T. These color maps indicate the quantity $B_1^{measured}/B_1^{nominal}$ in percentage terms. The maps in each column correspond to the same Q factor which is indicated at the top of each column. The maps in each row correspond to the same detuning efficiency which is written on the left side of each row. The simulated map below each experimental map corresponds to the same Q factor and detuning efficiency as the experimental map. For central slices, the imaging planes were located at the center of the circular-planar coil (symmetry plane of the coil, shown by dashed lines in Fig. 3(b)). In off-center slices, there was an offset of 12.5 mm between the imaging plane and the center of the coil. For both axial and coronal slices, the DE_{thr} of each coil is calculated using Eq. 12, and is written on the top of the corresponding column. Note that an accurate measurement of large detuning efficiencies is not possible if the Q factor is too low. Therefore in these cases the experimental maps are not available (see the results section for more explanation). Background noise in all experimental maps has been masked (pale blue).

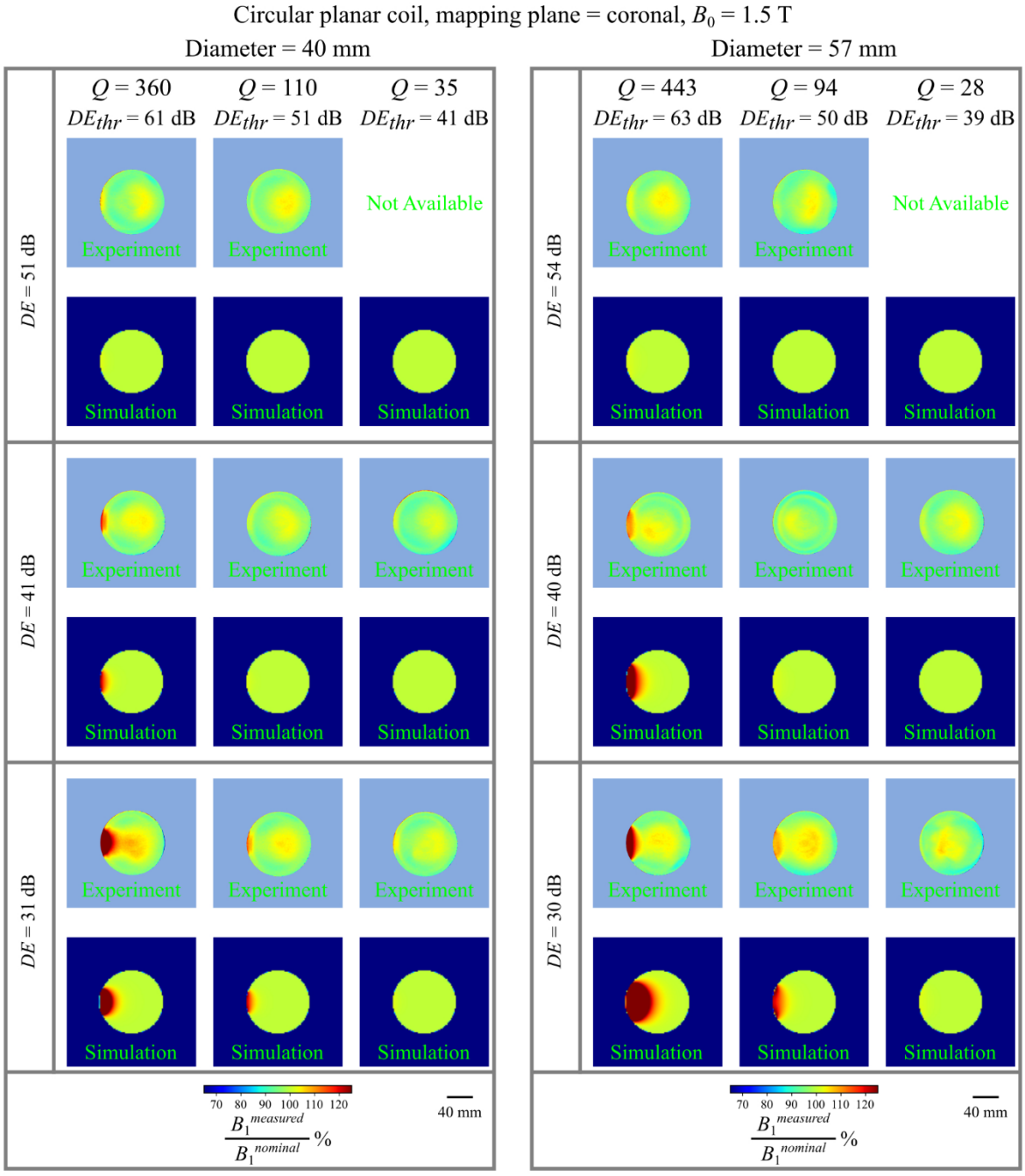

Figure 6: Experimental and simulated coronal B_1 maps for the 40 mm (left) and 57 mm (right) circular planar coils at 1.5 T. These color maps indicate the quantity $B_1^{measured}/B_1^{nominal}$ in percentage terms. The maps in each column correspond to the same Q factor which is indicated at the top of each column. The maps in each row correspond to the same detuning efficiency which is written on the left side of each row. The simulated map below each experimental map corresponds to the same Q factor and detuning efficiency as the experimental map. The corresponding DE_{thr} of each coil is calculated using Eq. 12, and is written on the top of the corresponding column. Note that an accurate measurement of large detuning efficiencies is not possible if the Q factor is too low. Therefore in these cases the experimental maps are not available (see the results section for more explanation). Background noise in all experimental maps has been masked (pale blue).

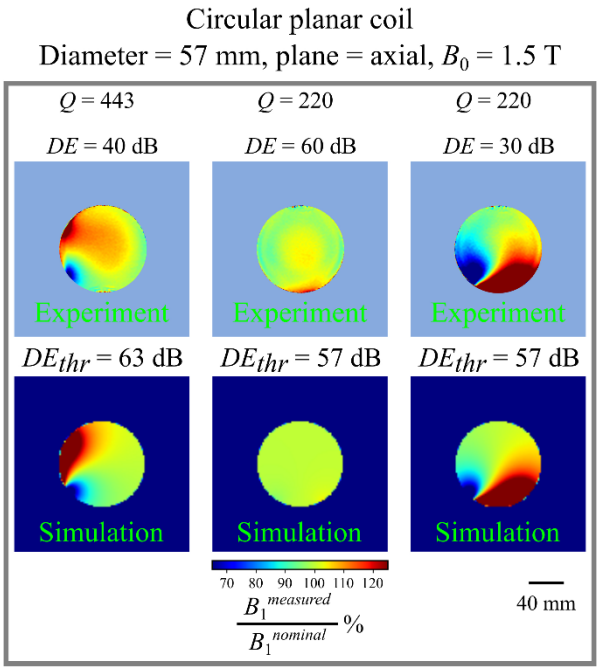

Figure 7: Experimental and simulated axial B_1 maps of the 57 mm circular planar coil at 1.5 T. These color maps indicate the quantity $B_1^{measured}/B_1^{nominal}$ in percentage terms. The Q factor, and detuning efficiency of each coil are indicated at the top of each column. The corresponding DE_{thr} of each coil is calculated using Eq. 12, and is written between the simulated and experimental maps. The simulated map below each experimental map corresponds to the same Q factor and detuning efficiency as the experimental map. Note that in the left column, the coil was at the left side of the phantom (and also the left side of the image), but in the middle and the right columns it was at the bottom of the phantom (and also the bottom of the image). Background noise in the experimental maps has been masked (pale blue).

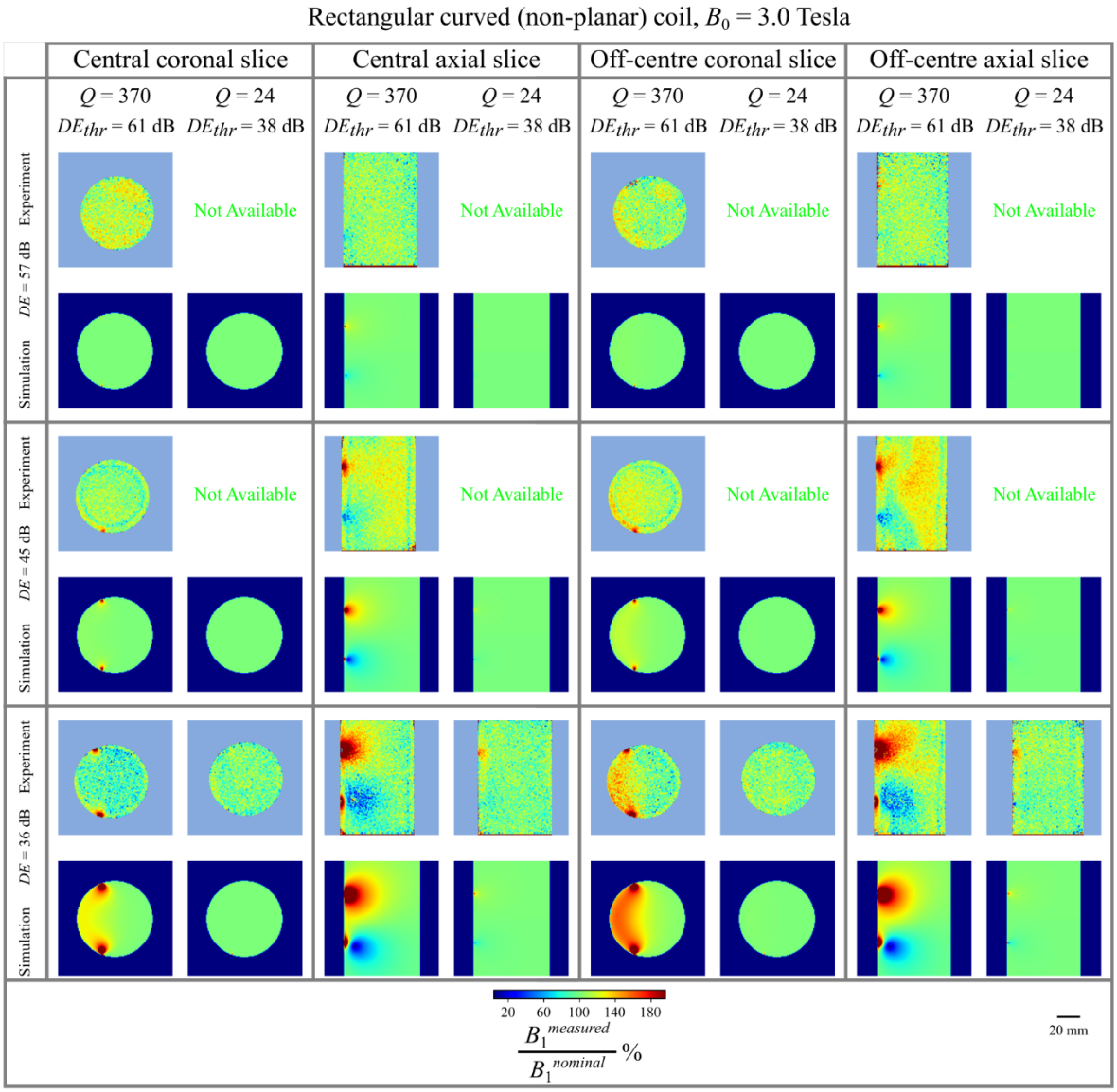

Figure 8: Experimental and simulated B_1 maps of the rectangular curved (non-planar) surface coil shown in Fig. 3(d) at 3.0 T. These color maps indicate the quantity $B_1^{measured}/B_1^{nominal}$ in percentage terms. The maps in each column correspond to the same Q factor which is indicated at the top of each column. The maps in each row correspond to the same detuning efficiency which is written on the left side of each row. The simulated map below each experimental map corresponds to the same Q factor and detuning efficiency as the experimental map. For central slices, the imaging plane was located at the center of the circular-planar coil (symmetry plane of the coil, shown by dashed lines in Fig. 3(d)). In off-center slices, there was an offset of 9.5 mm between the imaging plane and the center of the coil. For both axial and coronal slices, the DE_{thr} of each coil is calculated using Eq. 12, and is written on the top of the corresponding column. Note that an accurate measurement of large detuning efficiencies is not possible if the Q factor is too low. Therefore in these cases the experimental maps are not available (see the results section for more explanation). Background noise in the experimental maps has been masked (pale blue).

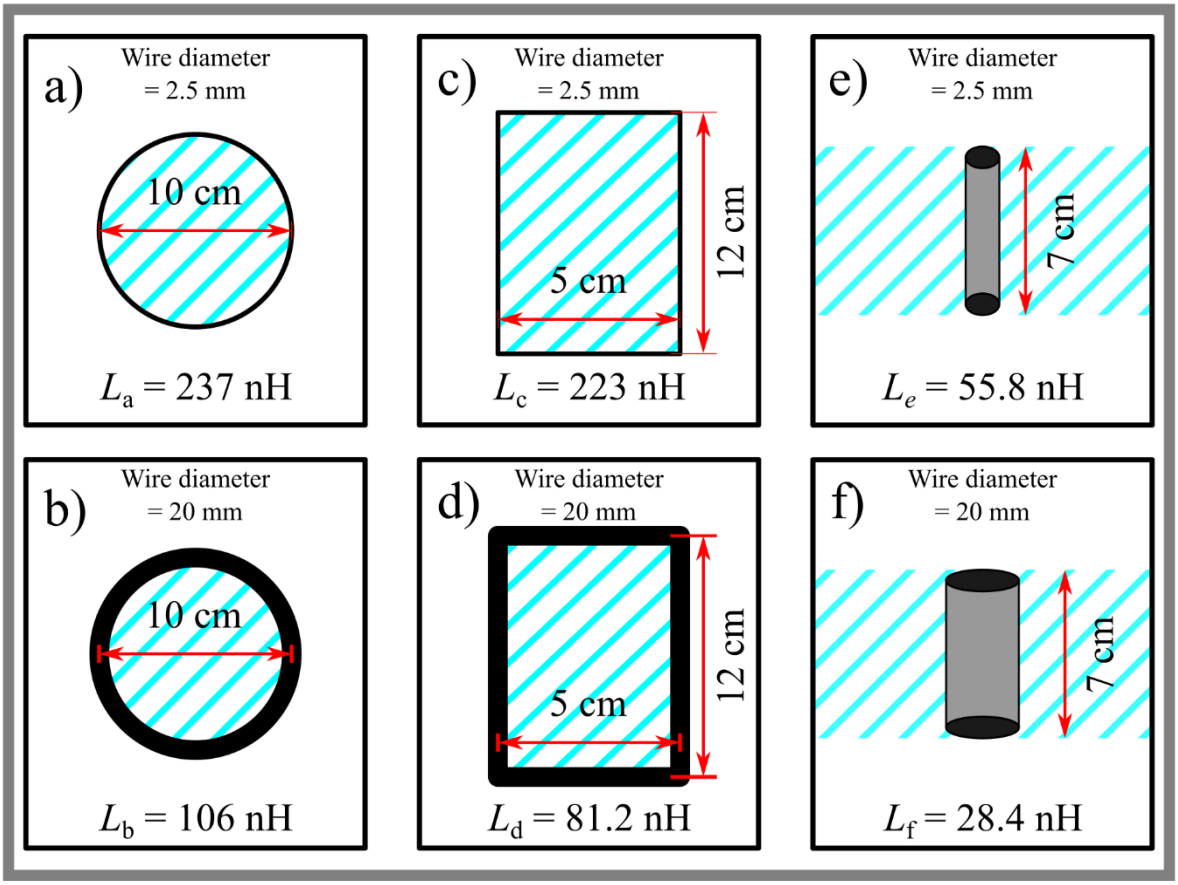

Figure 9: The illustration of three thin and thick structures used to estimate the parameter α. The conductor has a circular cross-section of 2.5 mm diameter (top) or 20 mm (bottom) in all structures. The inductance of each structure has been calculated using the inductance calculator freely provided by: https://www.eeweb.com.

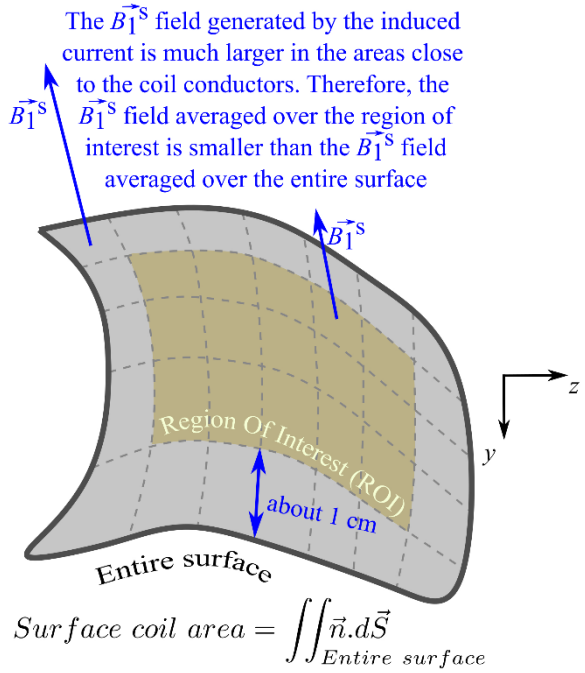

Figure 10: A surface coil with an arbitrary shape. The coil is positioned inside a volume transmit coil such that the primary $\vec{B}_1^{p,+}$ field of the transmit coil can induce a current. This induced current generates a secondary $\vec{B}_1^{s,+}$ field much larger in the areas close to the coil conductors. Note the large and small arrows indicating different amplitude and direction of $\vec{B}_1^s$ at different areas. Note that the *yz* view of the coil is shown for better illustration, which is different to that shown in Fig. 2(a).